

Deep Learning Predicts Biomarker Status and Discovers Related Histomorphology Characteristics for Low-Grade Glioma

Author Information

Zijie Fang^{1,†}, Yihan Liu^{2,†}, Yifeng Wang^{3,†}, Xiangyang Zhang^{2,†}, Yang Chen¹, Changjing Cai², Yiyang Lin¹, Ying Han², Zhi Wang¹, Shan Zeng², Hong Shen^{2,*}, Jun Tan^{4,*}, Yongbing Zhang^{5,*}

[†] These authors contributed equally.

^{*} Corresponding authors.

Affiliations

¹ Tsinghua Shenzhen International Graduate School, Tsinghua University, Shenzhen, China, 518055

² Department of Oncology, Xiangya Hospital, Central South University, Changsha, China, 410008

³ School of Science, Harbin Institute of Technology (Shenzhen), Shenzhen, China, 518055

⁴ Department of Neurosurgery, Xiangya Hospital, Central South University, Changsha, China, 410008

⁵ School of Computer Science and Technology, Harbin Institute of Technology (Shenzhen), Shenzhen, China, 518055

Contributions

Z.F., Y.Liu, Y.W., X.Z., Y.C., H.S, J.T., and Y.Z. designed the study. Y.Liu, X.Z., C.C., Y.H., and S.Z. collected the data and labels. Z.F., Y.W., Y.C., and Y.Lin implemented the pipeline. Z.F., Y.Liu, X.Z., and J.T. analyzed and interpreted the results. Z.F., Y.Liu, Y.W., X.Z., Y.Lin, Z.W., H.S., and Y.Z. drafted the manuscript. H.S., J.T., and Y.Z. supervised the study. All authors read and approved the final manuscript.

Corresponding authors

Correspondence to: Hong Shen (hongshen2000@csu.edu.cn); Jun Tan (tanjunsea@csu.edu.cn); Yongbing Zhang (ybzhang08@hit.edu.cn, primary contact).

Abstract

Biomarker detection is an indispensable part in the diagnosis and treatment of low-grade glioma (LGG). However, current LGG biomarker detection methods rely on expensive and complex molecular genetic testing, for which professionals are required to analyze the results, and intra-rater variability is often reported. To overcome these challenges, we propose an interpretable deep learning pipeline, a Multi-Biomarker Histomorphology Discoverer (Multi-Beholder) model based on the multiple instance learning (MIL) framework, to predict the status of five biomarkers in LGG using only hematoxylin and eosin-stained whole slide images and slide-level biomarker status labels. Specifically, by incorporating the one-class classification into the MIL framework, accurate instance pseudo-labeling is realized for instance-level supervision, which greatly complements the slide-level labels and improves the biomarker prediction performance. Multi-Beholder demonstrates superior prediction performance and generalizability for five LGG biomarkers (AUROC=0.6469-0.9735) in two cohorts (n=607) with diverse races and scanning protocols. Moreover, the excellent interpretability of Multi-Beholder allows for discovering the quantitative and qualitative correlations between biomarker status and histomorphology characteristics. Our pipeline not only provides a novel approach for biomarker prediction, enhancing the applicability of molecular treatments for LGG patients but also facilitates the discovery of new mechanisms in molecular functionality and LGG progression.

Introduction

Glioma is one of the most prevalent types of primary brain tumours¹. According to the World Health Organization's grading system, gliomas can be divided into four grades, among which low-grade glioma (LGG) includes grades below III². LGG, despite its slow growth, can still infiltrate normal tissues and

potentially relapse as high-grade gliomas even after treatment, the median overall survival of which is within 18 months after diagnosis³. Therefore, early screening and treatment are vital for LGG patients. Presently, biomarker detection plays a significant role in the clinical practice of LGG diagnosis and treatment⁴⁻⁶. On the one hand, biomarker status can assist pathologists in LGG subtyping. For instance, LGG cases with both isocitrate dehydrogenase (*IDH1/2*) mutation and *1p/19q* codeletion are diagnosed as oligodendrogliomas, which typically carry a favorable prognosis with longer progression-free survival^{7,8}. And the co-occurrence of *ATRX* mutation and *IDH1/2* mutation suggests a higher likelihood of astrocytoma^{8,9}. On the other hand, biomarker status helps plan treatments. Alkylating agent chemotherapy appears to be more effective in LGG patients with *1p/19q* codeletion¹⁰, and the methylation status of the *MGMT* promoter is a well-established predictive biomarker for determining the response to temozolomide¹¹.

In the routine clinical workflow for LGG biomarker detection, pathologists rely on biopsy samples of the lesion tissues for molecular testing¹². However, molecular testing commonly depends on wet laboratory techniques, including immunohistochemistry (IHC), fluorescence in-situ hybridization (FISH), polymerase chain reaction (PCR), deoxyribonucleic acid (DNA) sequencing, and others¹³⁻¹⁵. These methods typically require additional reagents and specialized equipment, and interpreting the test results demands professional personnel. These factors considerably impede the promotion of biomarker detection, especially in resource-limited regions¹⁶. Moreover, intra-rater inconsistency in the evaluation of detection results is frequently reported, resulting in resource wastage due to the requirement for re-testing^{17,18}. Furthermore, molecular detection methods usually require additional biopsy tissue beyond the standard diagnostic procedure^{16,19}. Consequently, biomarker detection is not feasible for LGG patients with tumors in hard-to-reach areas or essential brain regions, where extensive tissue removal is not possible²⁰. These issues in current biomarker detection methods further hinder the improvement of overall survival in LGG patients.

Since the Food and Drug Administration approved the use of whole slide imaging (WSI) in pathology in 2017, the digitalization of tissue slides has become a routine practice in tumor diagnosis^{21,22}. Coinciding with the explosive growth of WSIs and the vigorous development of artificial intelligence, the adoption of deep learning in automated pathological diagnosis and prognosis prediction has created an emerging field, computation pathology^{23,24}. Because pathology diagnosis is the definitive diagnosis, all LGG patients have hematoxylin-eosin (H&E) stained WSIs²⁵. Therefore, deep learning can remarkably reduce the cost and requirements of LGG biomarker detection by directly predicting the biomarker status with easily accessible H&E-stained WSIs, ultimately increasing the overall survival time of patients.

Nowadays, researchers have already applied deep learning to detect biomarkers in common cancers such as lung cancer²⁶, colorectal cancer^{27,28}, and breast cancer²⁹⁻³². Although some studies have achieved promising performance, very few focus on biomarker prediction in LGG due to the lack of data and fine-grained biomarker status labels. Some studies have utilized magnetic resonance imaging (MRI) images to determine the molecular mutation status in glioma patients^{20,33-35}. Nevertheless, MRI is not sensitive to early-stage lesions and cannot obtain sufficient anatomical details of the tumor due to lower resolution compared with WSIs. Therefore, some studies attempted to predict specific biomarkers such as *IDH1/2* mutation, *p53* mutation, and *MGMT* methylation status based on the limited pathological data³⁶⁻³⁸. However, there is still a lack of comprehensive and systematic prediction for widely used biomarkers in LGG. Besides, some methods were trained on the in-house dataset³⁸, which can hardly be accessed due to ethical and private issues. Furthermore, few of these studies concerned the interpretability of the proposed model. Deep learning models, with their large-scale parameters, introduce great complexity that poses challenges to understanding and interpreting the models. Enhancing the interpretability of deep learning models not only helps patients and pathologists trust the model's decision but also can facilitate the study of tumor progression and biomarker functionality.

To address the issues mentioned above, we propose a Multi-Biomarker Histomorphology Discoverer (Multi-Beholder) pipeline, which successfully predicts the status of five typical biomarkers in LGG, namely *1p/19q* codeletion, *ATRX* mutation, *TERT* promoter mutation, *IDH1/2* mutation, and *MGMT* promoter methylation, solely based on H&E-stained WSIs and slide-level labels (Fig. 1). Notably, as far as we know, this is the first time that the *1p/19q* codeletion, *ATRX* mutation, and *TERT* promoter mutation status have been successfully predicted using only H&E-stained WSIs. Specifically, we integrate one-class classification (OCC) into the multiple instance learning (MIL) framework to complement the coarse-grained supervision from the slide-level biomarker labels. OCC provides accurate fine-grained instance pseudo-labels as extra instance-level supervision, thus greatly improving the biomarker prediction performance. Furthermore, domain generalization (DG) is employed to enable the pipeline trained on the source domain to generalize to the target domain. To the best of our knowledge, we are the first to exploit OCC for the MIL framework in computation pathology. By incorporating Multi-Beholder with attention-based instance aggregation, our proposed pipeline is fully interpretable, which not only improves the reliability of the pipeline but also facilitates the clinicians in discovering the correlations between histomorphology patterns and biomarker status, ultimately promoting a better understanding of new mechanisms in biomarker functionality.

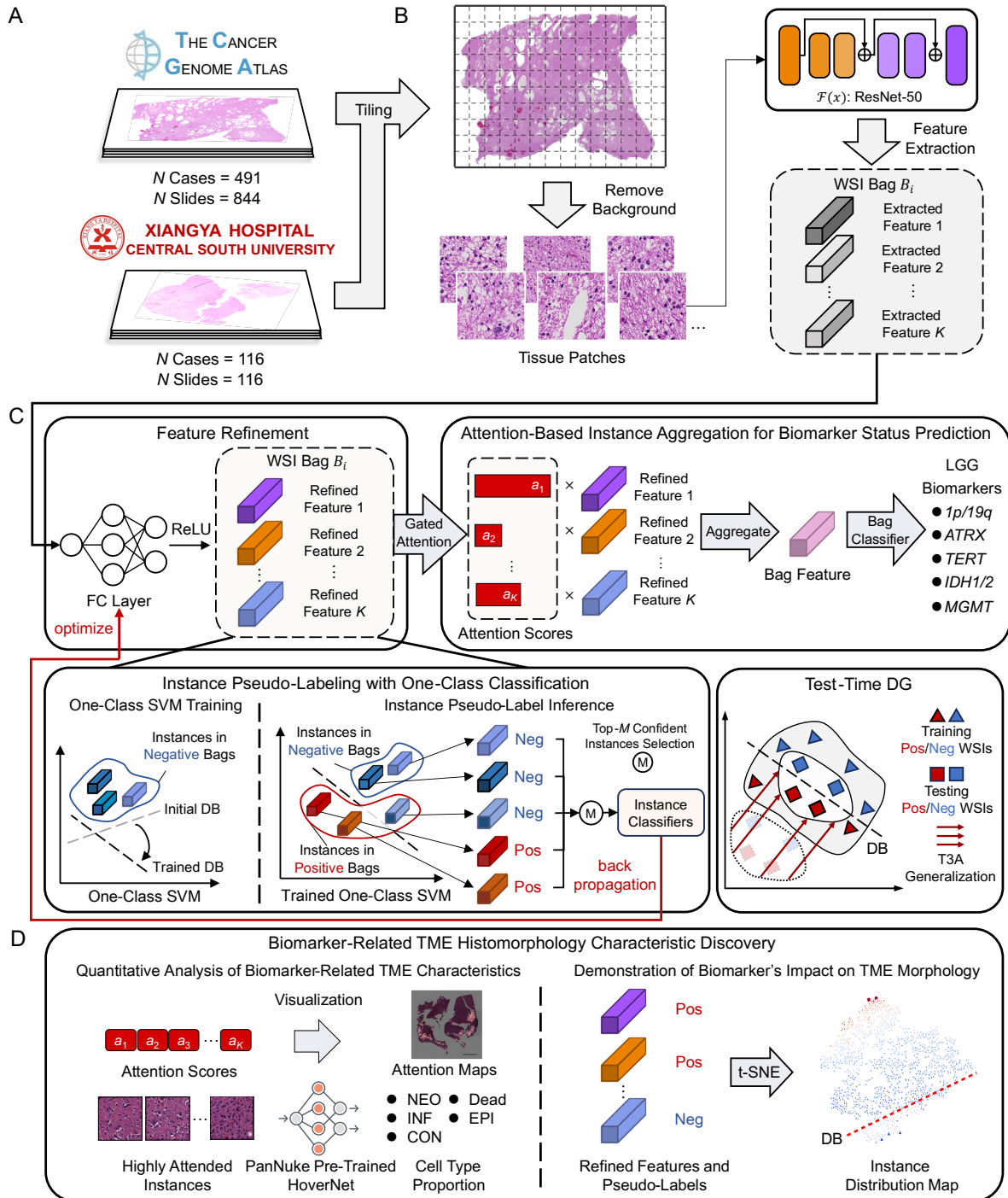
Results

Multi-Beholder pipeline overview and dataset characteristics

This paper proposes a fully automated pipeline named Multi-Beholder, which predicts the status of five common biomarkers in LGG, i.e., *1p/19q* codeletion, *ATRX* mutation, *TERT* promoter mutation, *IDH1/2* mutation, and *MGMT* promoter methylation, by using H&E-stained WSIs with slide-level labels. Since each WSI contains hundreds of millions of pixels, we cut the WSIs into non-overlapped equal-sized small patches to alleviate the memory burden on the graphic processing unit (GPU). Next, considering the labels

of the patches are unavailable, we adopt the MIL framework into the Multi-Beholder pipeline. The MIL framework treats WSIs as bags and image patches as instances, where the features of all the instances are aggregated to a bag feature, thereby enabling bag-level labels to supervise the whole pipeline. However, due to the limited number of WSIs in LGG datasets, only utilizing the supervision of bag-level labels is insufficient to achieve a satisfactory performance. Therefore, assigning pseudo-labels to the instances is usually necessary to obtain better instance-level features. It should be noted that the positive bags contain both positive and negative instances, but the negative bags contain only negative instances. To better use this property to improve the accuracy of pseudo-labels of instances in positive bags, we specifically introduce the OCC strategy into the MIL framework. The OCC strategy can exploit the true negative instances in negative WSIs to obtain a reliable negative-positive decision boundary, which is then utilized to assign accurate pseudo-labels to the instances in the positive bags. Compared with the bag-level labels, the instance pseudo-labels can assist the pipeline's learning process to enhance the discriminative ability of the instance features and ultimately improve the accuracy of the biomarker prediction task. Moreover, benefiting from the OCC's ability to better classify the negative and positive instances in positive bags, OCC enables the quantification of the impact of biomarker status on histopathological characteristics in the tumor micro-environment (TME), thereby promoting the clinical discovery of new mechanisms in LGG progression and molecular functionality. An overview of the Multi-Beholder pipeline is illustrated in Fig. 1. We train the Multi-Beholder pipeline on the TCGA-LGG dataset with a 10-fold Monte Carlo cross-validation. Besides, we build an external cohort named Xiangya by collecting H&E-stained WSIs and biomarker status of LGG patients from the Xiangya Hospital. Note that the stain protocol, scanners, and patient race in Xiangya differ from that of the TCGA-LGG dataset, thereby fully demonstrating the generalization ability of the Multi-Beholder. Details of the two datasets are summarized in Table. 1.

Fig. 1: An overview of the Multi-Beholder pipeline for LGG biomarker status prediction and biomarker-related TME histomorphology characteristic discovery.



A Data sources of the Multi-Beholder pipeline. The TCGA-LGG dataset, consisting of 844 WSIs from 491 cases, is utilized for training and cross-validation. The in-house Xiangya cohort consists of 116 cases, which are used for external validation. **B** The pre-processing of the Multi-Beholder pipeline. We first filter the background areas of each WSI and cut out patches with sufficient tissue areas. Then, we utilize an ImageNet pre-trained ResNet50 to convert each patch to a feature vector. **C** The workflow of biomarker status prediction. Firstly, the extracted patch features are fed into an instance feature refinement module. The instance feature refinement module introduces OCC, which only employs true negative instances in negative WSIs to obtain a reliable decision boundary of negative and positive instances, thereby distinguishing between negative and positive instances in positive WSIs for accurate instance pseudo-labeling. Finally, by aggregating all refined instance features based on the gated attention mechanism, a bag feature is obtained for biomarker status prediction. For better generalization, test-time template augmentation (T3A) is utilized for test-time DG. **D** A summary of the process to discover the biomarker-related TME histomorphology characteristics. We mask the attention maps on the WSIs to discover the most relevant histomorphology characteristics with the biomarker status. For quantitative analysis of the TME in highly attended patches, we utilize a HoverNet pre-trained on the PanNuke dataset to segment and classify cells in the patches, and the results are utilized to calculate the proportion of different cell types in the TME. Besides, we apply t-SNE to visualize the distribution of instance features, enabling an intuitive demonstration of the biomarker's influence on the TME morphology. WSI: whole slide image; FC: fully connected; DB: decision boundary; SVM: support vector machine; Neg: negative; Pos: positive; T3A: test-time template augmentation. NEO: neoplastic; INF: inflammatory; CON: connective; EPI: epithelial.

Multi-Beholder predicts *1p/19q* codeletion status and discovers correlated histomorphology characteristics

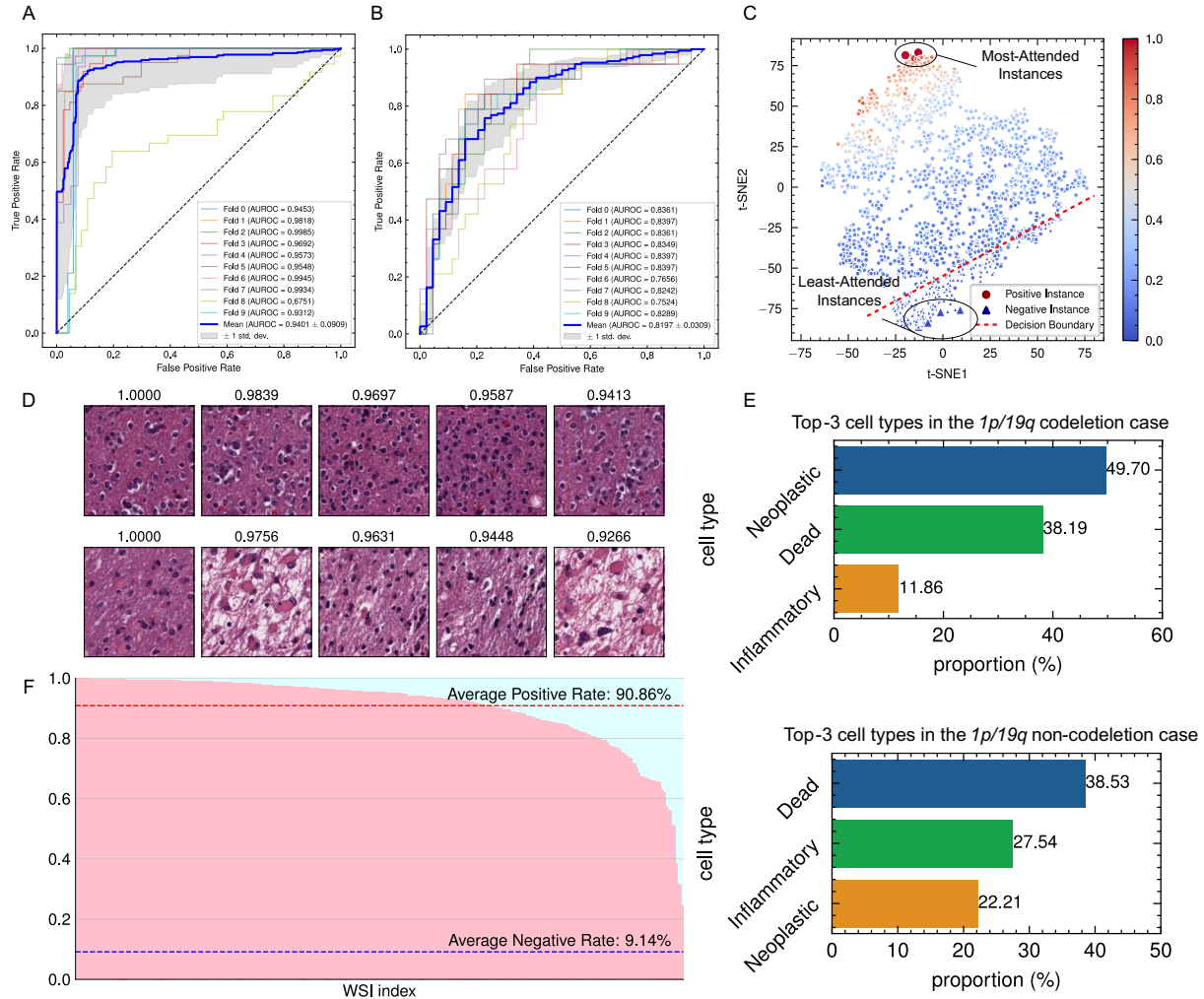
The *1p/19q* codeletion status is one of the most essential biomarkers for LGG patients. Previous studies have validated that LGG patients with *1p/19q* codeletion have better prognoses and higher sensitivity to chemotherapy with alkylating agents^{39,40}. To discover the relationship between *1p/19q* codeletion and histomorphology characteristics, we apply the Multi-Beholder pipeline to the TCGA-LGG dataset. Results show that the Multi-Beholder successfully classifies patients with and without *1p/19q* codeletion, achieving an AUROC (Area under Receiver Operating Curve) of 0.9401 ± 0.0909 (mean \pm std, Fig. 2A) on the test set with T3A. In terms of other metrics, the Multi-Beholder achieves excellent performance in accuracy (mean \pm std, 0.7869 ± 0.1237) and precision (mean \pm std, 0.8107 ± 0.1831). In addition, the recall (mean \pm std, 0.7509 ± 0.1327) and F1 score (mean \pm std, 0.7324 ± 0.1811) of the Multi-Beholder also exhibit satisfactory results (Supplementary Fig. 1A). To validate the generalization ability of the Multi-Beholder, we directly apply the Multi-Beholder trained on TCGA-LGG to the Xiangya cohort. External validation results prove that the Multi-Beholder has excellent generalization capability with an AUROC of 0.8197 ± 0.0309 , an accuracy of 0.7603 ± 0.0372 , an F1 score of 0.6404 ± 0.1138 , a recall of 0.6505 ± 0.0949 , and a precision of 0.7067 ± 0.1240 (Fig. 2B, Supplementary Fig. 1A).

Besides, the Multi-Beholder discovers the relationship between *1p/19q* codeletion and histopathological characteristics in TME. Attention visualization on a *1p/19q* codeletion case illustrates the dependencies between *1p/19q* codeletion and TME characteristics. In the attended regions, dense glial cells can be observed by darker staining, indicating *1p/19q* codeletion may lead to improved glial cell density in the TME (Supplementary Fig. 2A). The enlarged top 5 most attended regions further show that the perinuclear halo frequently appears, indicating its potential correlation with *1p/19q* codeletion (Fig. 2D). In comparison, the attention map of the case without *1p/19q* codeletion shows that glial cells are sparse with severe atypia. Besides, eosinophilic granular bodies and Rosenthal fibers can be observed, suggesting that they may indicate a lower probability of *1p/19q* codeletion (Fig. 2D, Supplementary Fig. 2B). To quantitatively reveal

the effect of *1p/19q* codeletion at a cell level, we further count the proportion of diverse cell types in the top 10% attended patches using a HoverNet⁴¹ (see "method"). Results show that the majority of the attended cells are neoplastic in the *1p/19q* codeletion case, with dead cells being the second majority. In comparison, in the *1p/19q* non-codeletion case, the dead cells appear the most frequently, with the second being inflammatory cells, which indicates more inflammatory reactions in LGG patients without *1p/19q* codeletion (Fig. 2E).

To study the impact of *1p/19q* codeletion on the global TME morphology, we uniformly select patches from the codeletion WSI and plot the patch features using t-SNE⁴² (Fig. 2C). We estimate the decision boundary of the OCC classifier by linear support vector regression⁴³ (SVR) (see "method"). The visualization demonstrates that almost all negative and positive instances are separated by the decision boundary rather than fused together. The most attended and least attended patches are located on the two corners of the plot, and instances with the same distances to the decision boundary have similar attention scores. These findings prove that the OCC classifier can effectively differentiate the negative and positive instances in the *1p/19q* codeletion WSI, even without patch-level labels. In addition, in the t-SNE plot, there are several instances below the decision boundary which are classified as negative, i.e., *1p/19q* non-codeletion. This phenomenon gives clues that a patient with *1p/19q* codeletion might have non-codeletion tissues, which indicates that the codeletion of *1p/19q* is in gradual progress rather than affects the whole TME morphology. We further calculate the proportion of positive and negative instances in all *1p/19q* codeletion WSIs. The quantitative result demonstrates that the *1p/19q* codeletion instances take up to 90.86% of areas in a positive WSI on average (Fig. 2F). These findings further validate that the impact of *1p/19q* codeletion on the TME has a localized characteristic.

Fig. 2: The Multi-Beholder predicts $1p/19q$ codeletion status in both TCGA-LGG and Xiangya cohort and discovers histomorphology correlations with the biomarker status.



A The Multi-Beholder successfully predicts the $1p/19q$ codeletion status on TCGA-LGG. The receiver operation curve (ROC) on the test dataset of each fold is plotted. **B** The ROCs of the Multi-Beholder when directly applying the pipeline trained on TCGA-LGG of each fold to the Xiangya cohort. **C** The t-SNE plot showing the distribution of the instance features in the $1p/19q$ codeletion case. The color represents the attention score of each instance, and the shape stands for the predicted label by the OCC classifier. Besides,

the most-attended and least-attended instances are enlarged in the plot. The red dashed line represents the estimated decision boundary of the OCC classifier by training a linear SVR on the dimension-reduced instance features. The negative instances below the boundary prove that *1p/19q* non-codeletion (negative) instances exist in the *1p/19q* codeletion (positive) WSI. **D** The five most attended instances in the *1p/19q* codeletion (upper) and non-codeletion (lower) case. The value on each patch represents the normalized attention score. In the codeletion case, high glial cell density can be observed together with clear perinuclear halos. In comparison, glial cells are sparse with severe atypia in the non-codeletion case, and eosinophilic granular bodies and Rosenthal fibers can be observed. **E** The proportion of different cell types predicted by a trained HoverNet in the top 10% attended patches of the *1p/19q* codeletion (upper) and non-codeletion (lower) case. The results show differences in cell type proportions between the codeletion and the non-codeletion case. **F** The proportion of positive and negative instances predicted by the OCC classifier in each positive WSI of the TCGA-LGG dataset. Each bar stands for a WSI, where red indicates positive instance proportion while blue stands for the negative. We sort the slide indexes by the positive instance proportion.

Multi-Beholder predicts the *ATRX* mutation and identifies biomarker-related histomorphology characteristics

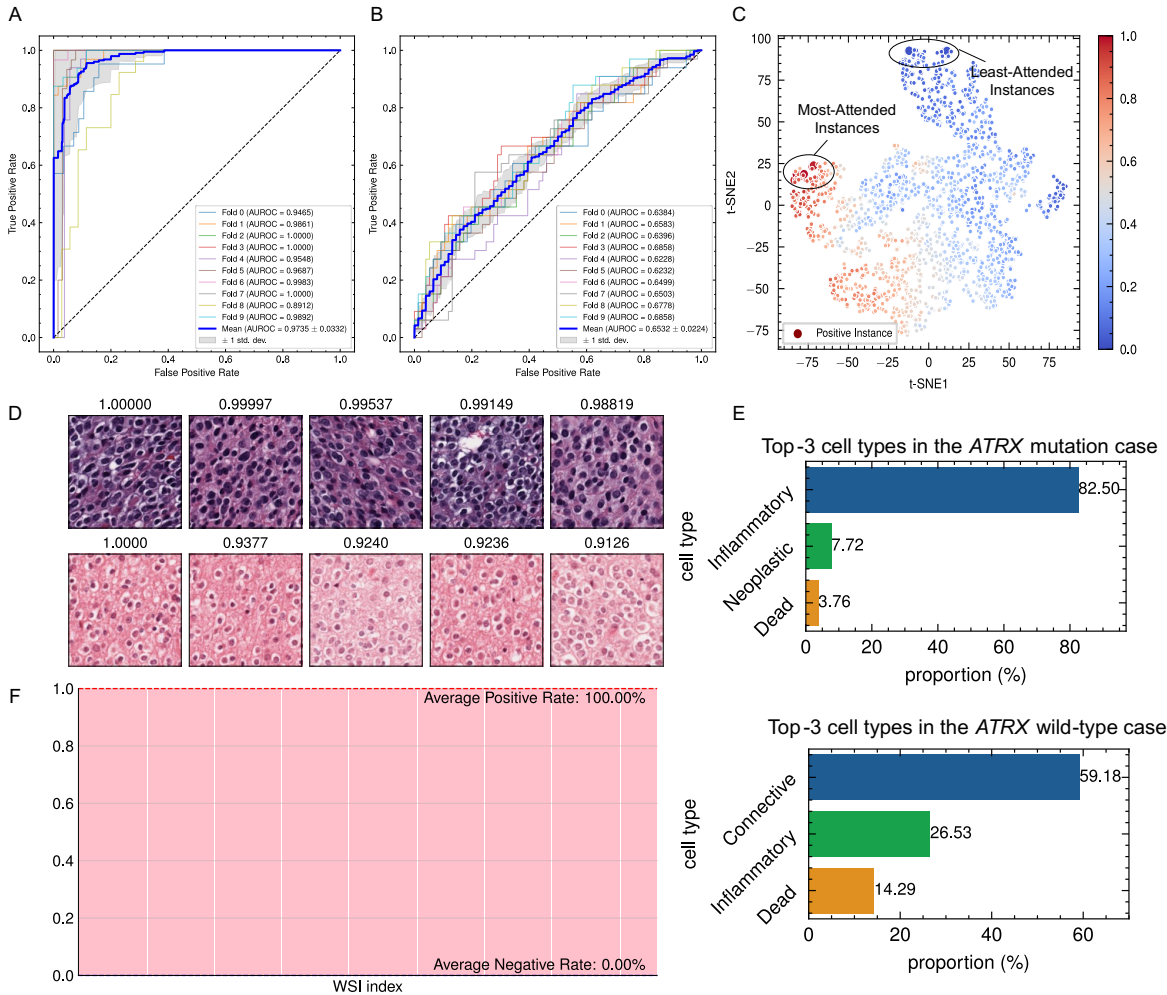
In the clinical subtyping of LGG, the *ATRX* mutation is a critical biomarker because it is more prevalent in diffuse astrocytoma. To eliminate the complex and time-consuming molecular testing methods for *ATRX* mutation, we apply the Multi-Beholder pipeline on the TCGA-LGG dataset. Results show that the developed Multi-Beholder achieves an average AUROC of 0.9735 ± 0.0332 (Fig. 3A) with T3A. In terms of other metrics, the Multi-Beholder reaches an accuracy of 0.7524 ± 0.1170 , F1 score of 0.6257 ± 0.1874 , recall of 0.6517 ± 0.1306 , and precision of 0.7387 ± 0.2362 (Supplementary Fig. 1B). By directly applying the trained Multi-Beholder to the Xiangya external cohort, the pipeline achieves an AUROC of

0.6532±0.0224, with an accuracy of 0.6055±0.0656, F1 score of 0.5679±0.0399, recall of 0.5928±0.0275, and precision of 0.5912±0.0363 under a 0.5 classification threshold (Fig. 3B, Supplementary Fig. 1B).

To discover the correlation between *ATRX* mutation and histomorphology, we apply attention maps on WSIs with mutated and wild-type *ATRX*, respectively (Supplementary Fig. 3). The most attended patches are enlarged for better visualization (Fig. 3D). The enlarged patches show that cell density is higher in *ATRX*-mutated WSI, with more severe cellular atypia, frequent nuclear divisions, and obvious perinuclear halos. But in the WSI with wild-type *ATRX*, cell distribution is looser with milder cellular atypia and microcysts can be observed. These findings indicate that *ATRX* mutation may have a close correlation with cellular atypia. Then, we utilize the HoverNet to calculate the different cell type proportions in the top 10% attended regions of the two WSIs (Fig. 3E). Quantitatively, the results demonstrate that inflammatory cells account for over 80% in the *ATRX*-mutated WSI, with a small number of neoplastic cells and dead cells. However, in the *ATRX* wild-type case, connective cells appear the most frequently, and inflammatory cells take up to 26.53% of all cells as well. These differences show that connective cells may be turned to inflammatory in *ATRX* mutation, and interactions among connective, inflammatory, and dead cells imply wild-type *ATRX*.

We further visualize the instance feature distributions in the *ATRX* mutation WSI using t-SNE to study the interrelationship between *ATRX* mutation and TME morphology (Fig. 3C). The high-attended and low-attended patch features are separated on the t-SNE plot, proving the effectiveness of feature refinement in the Multi-Beholder. In addition, it is very interesting to find that the trained OCC classifier predicts all patches in the WSI to be positive. Moreover, after we apply the OCC classifier to other *ATRX* mutation WSIs, we also find that all instances are predicted positive (Fig. 3F). This finding indicates that *ATRX* mutation has a global effect on the TME instead of extending from local tissue to the global, like that in *1p/19q* codeletion.

Fig. 3: The Multi-Beholder predicts the *ATRX* mutation status in TCGA-LGG and Xiangya cohort and identifies biomarker-related histomorphology characteristics.



A The Multi-Beholder successfully predicts the *ATRX* mutation status on TCGA-LGG. The ROC on the test dataset of each fold is plotted, with the mean ROC plotted in the thick blue line. The standard deviation is shown in grey shadows. **B** The ROCs of the Multi-Beholder trained on TCGA-LGG of each fold when applied to the Xiangya cohort. **C** The t-SNE plot of the distribution of instance features in the *ATRX* mutation case. The color represents the attention score, and the most-attended and least-attended instances

are enlarged in the plot. The plot shows that the OCC classifier classifies all instances in the WSI into the positive category. Therefore, there are no decision boundaries to be plotted. **D** The five most attended instances in the *ATRX* mutation (upper) and wild-type (lower) case. The value on the top of each patch represents the normalized attention score. In the *ATRX* mutation case, cells are relatively denser, with round-shaped nuclei and obvious perinuclear halos. Nuclear division can be observed. In the wild-type case, looser cell distribution with milder cellular atypia and microcysts is observed. **E** The proportion of different cell types predicted by a trained HoverNet in the top 10% attended patches of the *ATRX* mutation (upper) and wild-type (lower) case. **F** The proportion of positive and negative instances predicted by the OCC classifier in each *ATRX* mutation WSI in the TCGA-LGG dataset. Results show that all instances in the *ATRX* mutation WSIs are positive.

Multi-Beholder correlates *TERT* promoter mutation status with TME histomorphology characteristics

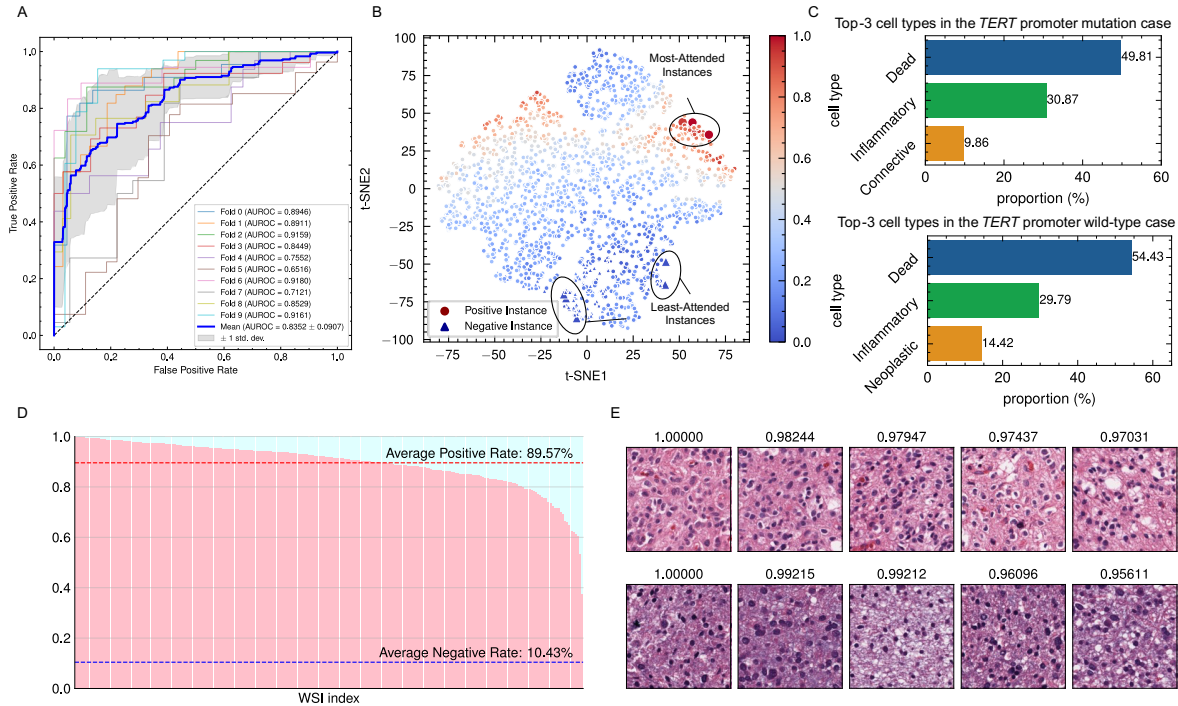
TERT promoter mutation is a critical biomarker in LGG diagnosis and treatment decisions, which is associated with a worse prognosis and decreased overall survival. We apply the Multi-Beholder to predict *TERT* promoter mutation status. Cross-validation results on the TCGA-LGG dataset show that the Multi-Beholder reaches an average AUROC of 0.8352 ± 0.0907 on the test sets (Fig. 4A). In terms of other metrics, Multi-Beholder achieves an accuracy of 0.7273 ± 0.1307 , an F1 score of 0.7079 ± 0.1621 , a recall of 0.7356 ± 0.1153 , and a precision of 0.7207 ± 0.1873 (Supplementary Fig. 1C).

Attention visualizations of the trained Multi-Beholder on a *TERT* promoter mutation case and a mutation-free case are illustrated (Supplementary Fig. 4). The attention map of the mutation case gives us insights that the highly attended regions have more aggregated glial cells (Supplementary Fig. 4A). From the enlarged attended instances, we discover that cell density is high with frequently appeared distinct

perinuclear halos and eosinophilic granules (Fig. 4E). In comparison, mild cellular atypia and nuclear division are observed in the most attended instances of the wild-type case (Fig. 4E, Supplementary Fig. 4B). The quantitative analysis using HoverNet implies that dead and inflammatory cells both act a key role in *TERT* promoter mutation and wild type, with a proportion of around 50% and 30%, respectively. However, connective cells substitute neoplastic cells in the *TERT* promoter mutation case for the third majority, giving clues that connective cells contribute to the formation of *TERT* promoter mutation (Fig. 4C).

Finally, we plot the patch features in the *TERT* promoter mutation WSI using t-SNE (Fig. 4B). The t-SNE plot shows that the instances with high attention scores and low attention scores are separated into two different clusters, which validates the discriminative ability of the refined features in the Multi-Beholder. Besides, both positive and negative instances exist in the *TERT* promoter mutation WSI, which is similar to the case in the *1p/19q* codeletion. It is worth noting that the number of negative instances is too few to train a linear SVR for estimating the boundary line, so it is not drawn in Fig. 4B. Furthermore, we find that the positive instances take up to 89.57% among all the patches by calculating the ratio of positive and negative instances in each *TERT* promoter mutated WSI (Fig. 4D). This phenomenon indicates that the *TERT* promoter mutation affects the tissue morphology gradually other than at a large scale at once.

Fig. 4: The Multi-Beholder predicts the *TERT* promoter mutation status in TCGA-LGG and discovers biomarker-related histomorphology characteristics.



A The Multi-Beholder successfully predicts the *TERT* promoter mutation status on TCGA-LGG. The ROC on the test dataset of each fold is plotted, with the mean ROC plotted by the thick blue line. The standard deviation is shown in grey shadows. **B** The t-SNE plot of the instance feature distribution in the *TERT* promoter mutation case. The color represents the attention score of each instance. The shape stands for the predicted category of the OCC classifier. Besides, the most-attended and least-attended instances are enlarged in the plot. The negative instances are too few to train a linear SVR for estimating the boundary line, so it is not plotted. **C** The proportion of the top three frequently appeared cell types within the top 10% attended patches in the *TERT* promoter mutation (upper) and wild-type (lower) WSI. **D** The proportion of positive and negative instances predicted by the trained OCC classifier in each *TERT* promoter mutation WSI of the TCGA-LGG dataset. Each bar in the figure represents a WSI, with red standing for the positive

instance ratio and blue being the negative instance ratio. **E** The five most attended instances in the *TERT* promoter mutation (upper) and wild-type (lower) case. The value on the top of each patch represents the normalized attention score. Glial cells are frequently aggregated in the mutation case, but mild cellular atypia and nuclear division are observed in the wild-type case.

Multi-Beholder predicts the *IDH1/2* mutation status with high generalization and discovers mutation-related TME morphology

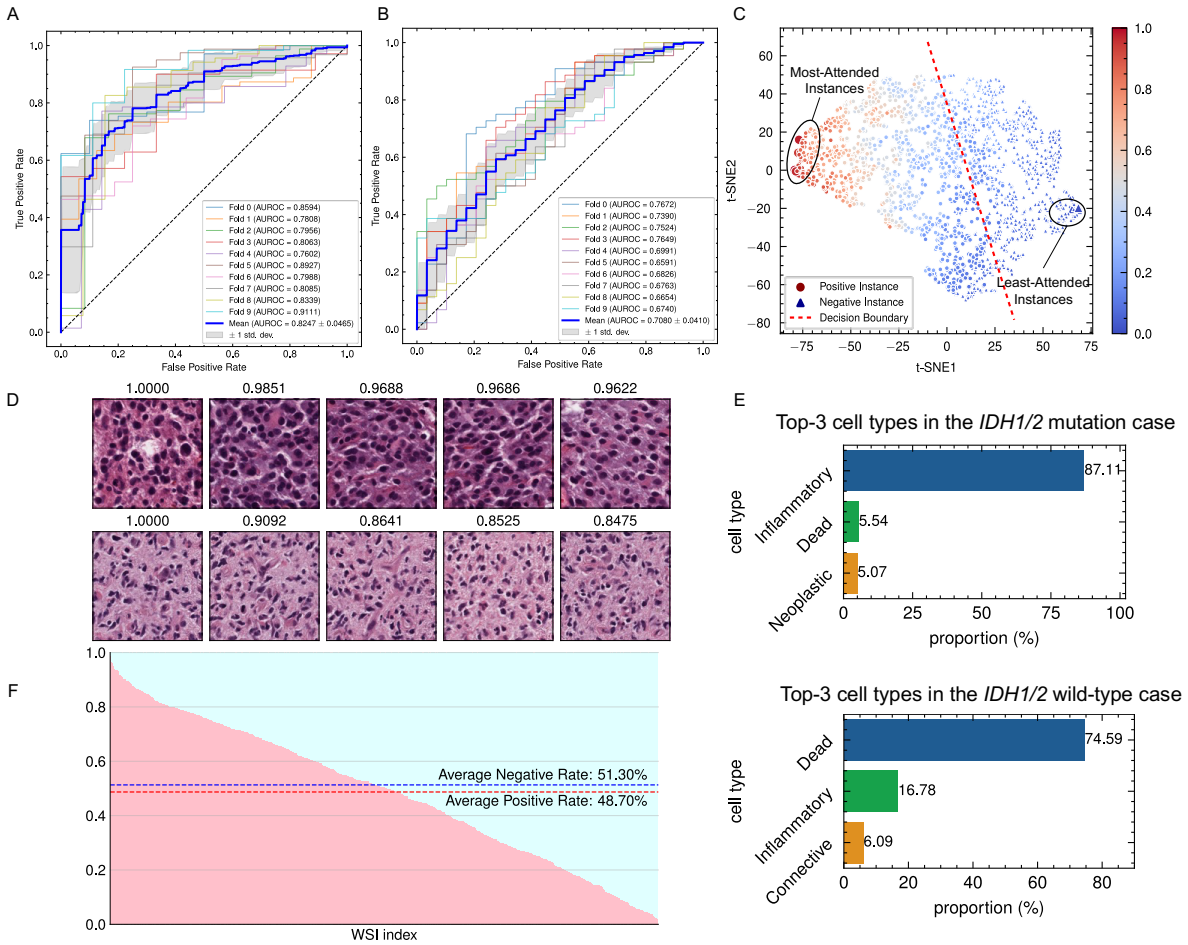
IDH1/2 mutation in LGG leads to the conversion of *IDH1/2* enzyme to a new active form named 2-hydroxyglutarate, which interferes with the normal metabolic process in cells and affects DNA methylation modification, leading to abnormal cell proliferation and tumor formation. Therefore, *IDH1/2* has been a critical biomarker in LGG diagnosis and prognosis. We apply the Multi-Beholder pipeline to predict the *IDH1/2* mutation status using the TCGA-LGG dataset and validate the trained pipeline on the Xiangya external cohort. Results on the TCGA-LGG dataset prove the strong prediction ability of the Multi-Beholder for *IDH1/2* mutation. The Multi-Beholder achieves an AUROC of 0.8247 ± 0.0465 (Fig. 5A). In terms of other metrics, the Multi-Beholder reaches 0.8490 ± 0.0456 , 0.6053 ± 0.0900 , 0.6166 ± 0.0848 , and 0.6907 ± 0.1733 in accuracy, F1 score, recall, and precision under a 0.5 classification threshold, respectively (Supplementary Fig. 1D). We then directly apply the trained Multi-Beholder to the Xiangya cohort. Results show that the Multi-Beholder still obtains an average AUROC of 0.7080 ± 0.0410 (Fig. 5B). Other metrics also validate the generalization ability of the Multi-Beholder (Supplementary Fig. 1D).

Attention visualizations of the trained Multi-Beholder on an *IDH1/2* mutation case and an *IDH1/2* wild-type case are illustrated (Supplementary Fig. 5). The attention map of the *IDH1/2* mutation case gives us insights that the Multi-Beholder treats high cell density as the evidence for *IDH1/2* mutation

(Supplementary Fig. 5A). Enlarging the top five attended patches further validates that the cell density is significantly high with severe nuclear atypia and cells in the mitotic phase appear frequently (Fig. 5D). In comparison, eosinophilic granular bodies are more frequently observed in the most attended patches of the *IDH1/2* wild-type case (Fig. 5D, Supplementary Fig. 5B). We then apply the HoverNet to segment and count the proportion of different cell types in the top 10% attended patches (Fig. 5E). It can be found that inflammatory cells compose 87.11% of the cells in the *IDH1/2* mutation case, while the proportion is only 16.78% in the wild-type case. In comparison, dead cells are the major cell type in the *IDH1/2* wild-type case, taking up to 74.59%. In addition, neoplastic cells replace connective cells in the *IDH1/2* mutation case as the third place. This phenomenon may indicate that the immune response is stronger in *IDH1/2* mutation, and tissue necrosis has a correlation with wild-type *IDH1/2*.

Besides, we plot the dimension-reduced patch features in the WSI with *IDH1/2* mutation using t-SNE (Fig. 5C). From the figure, we can find that the instances with similar attention scores share similar distances to the OCC classifier's estimated decision boundary, and the most-attended and least-attended instances are located on the two ends of the plot, which validates the effectiveness of the Multi-Beholder. Furthermore, the figure shows that the number of *IDH1/2* mutation patches and wild-type patches is nearly the same. Quantitative results also prove that the number of *IDH1/2* mutation patches and wild-type patches is almost 1:1 (Fig. 5F). These results indicate that the impact of *IDH1/2* mutation on the TME is limited in a local region other than affects the tissue morphology at a global scope.

Fig. 5: The Multi-Beholder predicts the *IDH1/2* mutation status in both TCGA-LGG and Xiangya cohort and discovers related TME morphologies.



A The Multi-Beholder successfully predicts the *IDH1/2* mutation status on TCGA-LGG. The ROC on the test dataset of each fold is plotted. **B** The ROCs of the Multi-Beholder when directly applying the model trained on TCGA-LGG of each fold to the Xiangya cohort. **C** The t-SNE plot of the distribution of instance features in the *IDH1/2* mutation case. The color represents the attention score, and the shape stands for the predicted label by the OCC classifier. Besides, the most-attended and least-attended instances are enlarged in the plot. The red dashed line is the estimated decision boundary of the OCC classifier in the t-SNE

dimension-reduced instance feature space. **D** The five most attended instances in the *IDH1/2* mutation (upper) and wild-type (lower) case. The value on the top of each patch represents the normalized attention score. High cell density is observed with severe nuclear atypia, and cells are frequently in the mitotic phase in the mutation case. In the wild-type case, eosinophilic granular bodies are observed. **E** The proportion of the top three frequently appeared cell types within the top 10% attended patches in the *IDH1/2* mutation (upper) and wild-type (lower) WSI. **F** The proportion of predicted positive and negative instances in each *IDH1/2* mutation WSI of the TCGA-LGG dataset. Each bar represents a WSI, with red standing for the *IDH1/2* mutated instance ratio and blue being the wild-type instance ratio.

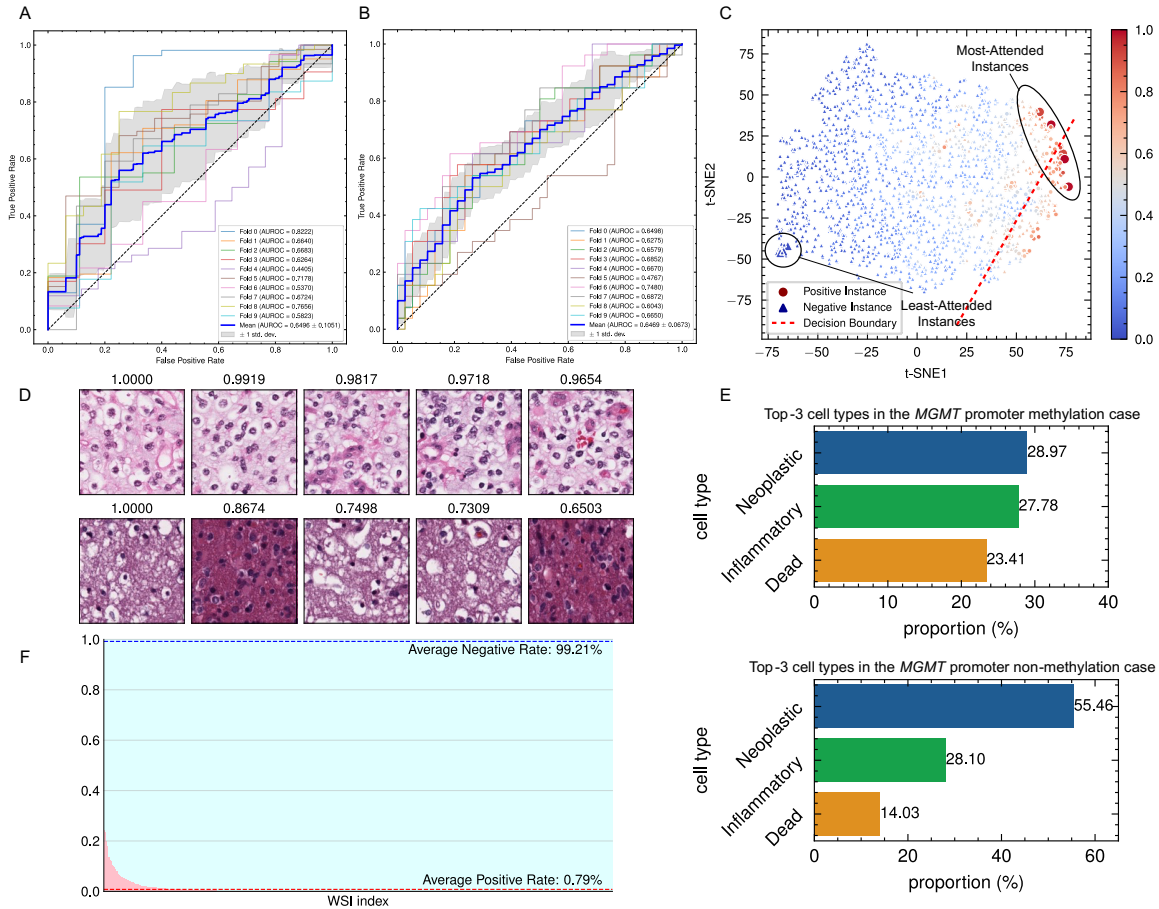
Multi-Beholder predicts the *MGMT* promoter methylation status and discovers methylation-related TME characteristics

MGMT promoter methylation status has been proven to have the capability to predict the risk of hypermutation at recurrence, and temozolomide is validated to have a better outcome for LGG patients with *MGMT* promoter methylation¹¹. To get rid of the complex testing process of *MGMT* promoter methylation, we adopt the Multi-Beholder to the TCGA-LGG and Xiangya cohort. Results show that the Multi-Beholder achieves an average AUROC of 0.6496 ± 0.1051 on the TCGA-LGG dataset and an AUROC of 0.6469 ± 0.0673 when directly applied to the external Xiangya cohort (Fig. 6A, B). In addition, the Multi-Beholder obtains an accuracy of 0.6372 ± 0.2039 , an F1 score of 0.4931 ± 0.1281 , a recall of 0.5803 ± 0.1051 , and a precision of 0.5621 ± 0.0862 on the TCGA-LGG dataset, and the metrics of the Multi-Beholder on the Xiangya cohort are similar to those on the TCGA-LGG dataset (Supplementary Fig. 1E). It is worth noting that the classification threshold for the *MGMT* promoter methylation is set to 0.8 due to the label imbalance, where 0.8 is determined by the approximate ratio of the *MGMT* promoter methylation WSIs to all WSIs in the TCGA-LGG dataset.

We next show the global attention visualization maps of the trained Multi-Beholder on an *MGMT* promoter methylation case and a methylation-free case (Supplementary Fig. 6). The five most attended instances are further enlarged (Fig. 6D). Denser distribution of glial cells can be observed in attended instances in the methylated WSI. Besides, eosinophilic granular bodies and glial microcysts are more frequently observed, with more severe cellular atypia and perinuclear halos. In comparison, nuclear division is frequently observed for the five most attended instances in the case without *MGMT* promoter methylation, with background tissue loosening that leads to microcyst formation. The HoverNet cell segmentation and classification results show that neoplastic, inflammatory, and dead cells all frequently exist in *MGMT* promoter methylation and wild-type cases, but the proportion of cell types is different (Fig. 6E). In general, the ratio of neoplastic cells is smaller in the methylated case than the non-methylated case, but the dead cells appear more frequently in the case with *MGMT* promoter methylation, which gives evidence that *MGMT* promoter methylation has a relationship with tumor cell death.

The patch features in the *MGMT* promoter methylation WSI are further visualized in Fig. 6C by t-SNE. Compared with other biomarkers, we find that the number of positive instances in the *MGMT* promoter methylated WSIs is much smaller. Almost all instances are labeled as negative, i.e., without *MGMT* promoter methylation. The quantitative result by calculating the ratio of positive and negative instances in each methylated WSI also proves this finding. On average, the proportion of positive instances in an *MGMT* promoter methylation WSI is only 0.79% (Fig. 6F). These findings indicate that *MGMT* promoter methylation influences the TME subtly. Accompanied by the findings in cell type proportion, we may draw the conclusion that *MGMT* promoter methylation only changes the proportion of different cell types. This effect may explain why Multi-Beholder performs not so well (average AUROC < 0.7) on the test dataset since it is easier for a model to detect the changes in cell types (similar to a classification task) than count the cell proportion, which is more closed to a dense detection task.

Fig. 6: The Multi-Beholder predicts the *MGMT* promoter methylation status in TCGA-LGG and Xiangya cohort and discovers correlated TME characteristics.



A The Multi-Beholder predicts the *MGMT* promoter methylation status on TCGA-LGG. The ROC on the test dataset of each fold is plotted. The mean ROC is plotted by the thick blue line, with the standard deviation shown in grey shadows. **B** The ROCs of the Multi-Beholder applied to the Xiangya cohort after training on each fold of the TCGA-LGG dataset. **C** The t-SNE plot of the instance feature distribution in the *MGMT* promoter methylated case. The color represents the attention score of each instance, and the shape indicates the predicted label by the OCC classifier. Besides, the most-attended and least-attended instances are enlarged in the plot. The red dashed line is the linear SVR-estimated decision boundary of the

OCC classifier on the t-SNE dimension-reduced feature space. **D** The five most attended instances in the *MGMT* promoter methylation (upper) and non-methylation (lower) case. The value on each patch represents the normalized attention score. Eosinophilic granular bodies and glial microcysts can be more frequently observed in the methylation case, with more severe cellular atypia and perinuclear halos. Comparatively, nuclear division is frequently observed with background tissue loosening that leads to microcyst formation in the non-methylation case. **E** The proportion of the top three frequently appeared cell types within the top 10% attended patches in the *MGMT* promoter methylation (upper) and non-methylation (lower) WSI. **F** The proportion of predicted positive and negative instances in each *MGMT* promoter methylated WSI of the TCGA-LGG dataset. Each bar in the figure represents a WSI, with red standing for the promoter methylated instance ratio and blue being the non-methylated instance ratio.

Discussion

Biomarkers play a significant role in the progression of LGG, and the subtyping and treatment of LGG patients heavily rely on the biomarker status. For instance, patients with *ATRX* mutation have a higher probability of having diffuse astrocytoma. In addition, previous studies have indicated that LGG patients with *IDH1/2* mutation and *1p/19q* codeletion tend to have a favorable prognosis⁴⁴, and patients with *MGMT* promoter methylation can benefit from the alkylating agents⁴⁵. Therefore, biomarker detection is an indispensable step in the diagnosis and treatment of LGG patients.

In the current LGG treatment, biomarker detection is usually conducted by molecular genetic testing methods such as PCR and FISH. However, these methods have quite a number of issues. For PCR, as an example, it requires strict experimental conditions and multiple steps, including DNA extraction, primer design, and temperature control, which need not only specifically built laboratories but also technical personnel. These limitations make biomarker detection very complex, expensive, and hard to equip, especially in resource-limited regions.

To overcome the above issues, we proposed a fully interpretable deep learning pipeline, Multi-Beholder, to predict the status of five substantial biomarkers in LGG with only H&E-stained WSIs. Given the giga-pixel-sized WSIs, we split the WSIs into small patches to satisfy the GPU memory capacity. However, the labels for the patches are not available. To this end, the Multi-Beholder aggregated all patch features in a WSI into a bag-level feature under the MIL framework, enabling supervision by the bag-level label. However, using bag labels alone may obtain unsatisfactory instance features, resulting in poor performance for biomarker prediction. To address this problem, we devised a pseudo-labeling method for instances and improved the accuracy of instance features under the supervision of the assigned pseudo-labels. Considering the instances in negative WSIs have accurate negative labels, we utilized the OCC strategy to fully exploit the true negative instances in negative WSIs and obtain a separable positive-negative decision boundary with high accuracy. Therefore, instances in positive bags can be clearly separated by the decision boundary, resulting in accurate instance-level pseudo-labels. Eventually, the instance-level supervision was utilized to refine the instance features, and the bag feature aggregated by the refined instance features could be more discriminative, thus achieving accurate biomarker prediction. To the best of our knowledge, we were the first to leverage OCC to label the instances in WSIs, which created a new way for instance pseudo-labeling in the MIL framework. To enhance the generalization of the Multi-Beholder, we further adopted the test-time template augmentation (T3A) strategy, which enabled the Multi-Beholder to adapt to test WSIs without retraining the model.

To prove the effectiveness of the Multi-Beholder, we cross-validated the Multi-Beholder on the public TCGA-LGG dataset and tested the model on the external Xiangya cohort, in which the staining protocol and scanners were different from those of TCGA-LGG. The results demonstrated that the Multi-Beholder could predict the status of five biomarkers in LGG, i.e., *1p/19q* codeletion, *ATRX* mutation, *TERT* promoter mutation, *IDH1/2* mutation, and *MGMT* promoter methylation, with high performance and generalization. Specifically, the results showed that the Multi-Beholder achieved an average AUROC of 0.9401, 0.9735,

0.8352, 0.8247, and 0.6496 for *1p/19q* codeletion, *ATRX* mutation, *TERT* promoter mutation, *IDH1/2* mutation, and *MGMT* promoter methylation on the TCGA-LGG dataset, respectively (Fig. 2-6A). External validation results on the Xiangya dataset also proved the generalization ability of the Multi-Beholder for the prediction of *1p/19q* codeletion, *ATRX* mutation, *IDH1/2* mutation, and *MGMT* promoter methylation.

Considering the clinical significance of the Multi-Beholder, it can be utilized as a complement to the current molecular detection methods. When applying the Multi-Beholder to the clinical LGG treatment process, clinicians can set a classification threshold to obtain a high recall to avoid missed detections, and only patients predicted positive by the Multi-Beholder are further applied with the molecular detection methods. Therefore, a large number of patients will not have to take complex molecular tests, and the workload of pathologists and expenditure of patients can be decreased. Hopefully, Multi-Beholder can obtain a better performance after delicate optimization and hyper-parameter tuning, with which the traditional detection methods can be fully substituted, and the clinical practice can be revolutionized.

Furthermore, our pipeline could automatically discover the TME characteristics that contributed the most to the biomarker status, which gave clues and laid the foundations for further research on the mechanism of LGG biomarkers. Specifically, the Multi-Beholder discovered the correlation between histomorphology and biomarker status on both a patch level and a slide level by visualizing the attention map. Additionally, quantitative analysis of the biomarkers' effect at a cell level was also enabled with a pre-trained HoverNet. Through the analysis of the attention maps, we found that the most attended instances were majorly tumor tissues, where the glial cells were denser, and the cell atypia was more substantial. Besides, more distinctive features such as mitoses, which represent cellular atypia, existed in most attended instances. These discoveries indicate that our model could analyze biomarker status through the morphological structure of glial cells and areas with high malignancy, which provides new ideas for the analysis of biomarkers based on TME morphology. By quantitatively calculating the proportion of different cell types in the most attended patches, we further found that the cell compositions of TMEs with different biomarker status had

different characteristics. For example, interactions between neoplastic and dead cells occurred in *1p/19q* codeletion cases, and inflammatory cells tended to replace the connective cells as the majority in the *ATRX* mutation case compared with the wild-type case.

In addition, benefiting from the OCC's ability to accurately classify negative and positive instances, we studied the proportion of negative to positive instances in the positive WSIs both qualitatively and quantitatively. Results demonstrated that although some cases were with *1p/19q* codeletion, *TERT* promoter mutation, or *IDH1/2* mutation, there were still some instances predicted negative. Considering these biomarkers should also be negative in healthy people's tissue morphology, this phenomenon may indicate that the *1p/19q* codeletion, *TERT* promoter mutation, and *IDH1/2* mutation are developed in a gradual process and influence the tissue morphology in a step-wise characteristic (Fig. 2C, F, Fig. 4C, F, and Fig. 5C, F). However, all instances were classified as positive by the OCC classifier in the *ATRX* mutation, indicating that mutations in the *ATRX* may have a global impact on the TME (Fig. 3C, F). Furthermore, almost all instances were predicted negative in the *MGMT* promoter methylation WSIs, giving clues that the *MGMT* promoter methylation has a very subtle effect on the tissue morphology of LGG. These discoveries can improve clinicians' understanding of the progression pattern of the LGG biomarkers and their impact on the TME characteristics. Combined with the attention visualizations, tissue regions that are highly correlated with the biomarkers can be identified, which has the potential to facilitate clinicians and pathologists for future studies of biomarker functionality and tumorigenesis mechanisms, ultimately helping the development of target therapy.

There are a few limitations in our study. Firstly, we only utilized the H&E-stained WSIs for training. Although pathological diagnosis based on H&E-stained slides is the gold standard for cancer diagnosis, many patients are screened with radiology like magnetic resonance imaging and computerized tomography. Utilizing multi-modality data may bring about better prediction performance, and exploring the relationship between different image modalities and the biomarker status may bring new findings on LGG progression.

Secondly, because the prediction of biomarker status in LGG is a novel research area, it was hard to get sufficient cases with biomarker status labels. As a result, the volume of the dataset was limited. The TCGA-LGG dataset used for training was less than 1,000 WSIs. The external Xiangya dataset had less than 120 cases where some biomarkers, like the *TERT* promoter mutation status, were not available. Although the results validated the excellent performance of the Multi-Beholder both on the TCGA-LGG dataset and the Xiangya dataset, the performance could be further improved with larger data size.

In summary, this paper proposed a deep learning pipeline named Multi-Beholder. To the best of our knowledge, we were the first to introduce the OCC strategy into the MIL framework to assign accurate pseudo-labels to the instances in the WSIs. The instance pseudo-labels were further utilized to refine the instance features, thereby improving the prediction accuracy of five common and useful biomarkers for LGG, among which the *1p/19q* codeletion, *ATRX* mutation, and *TERT* promoter mutation status was predicted by WSIs for the first time. Besides, our pipeline successively discovered the correlations between biomarker status and TME histomorphology from a cell level to a global perspective, helping future research on the functionality of LGG biomarkers. Our pipeline can also be easily extended to other tumors for biomarker prediction and biomarker-related histomorphology characteristic discovery, which may revolute the current tumor diagnosis and treatment process by substituting the traditional molecular detection methods.

Methods

Data Sources and Pre-Processing

Public TCGA-LGG Dataset

We collected 844 WSIs from 491 cases diagnosed with LGG in The Cancer Genome Atlas Program to build the TCGA-LGG dataset. All the WSIs were scanned in the SVS format. In the dataset, most cases (n=379) only had one WSI, while a few cases had multiple WSIs, with a maximum of 17 WSIs per case.

For cases with multiple WSIs, we assumed that the biomarker labels of all WSIs were consistent with the biomarker status of the case. For each WSI, we followed the pre-processing pipeline in CLAM⁴⁶, which first used the OTSU⁴⁷ method to segment the background areas and divided each WSI into 256×256 -shaped patches under a $20\times$ magnification (mpp=0.5). A WSI was discarded if the tissue area in the WSI was too tiny (without any continuous tissue areas larger than 4096×4096 under $40\times$). After pre-processing, we had 831 WSIs from 485 cases. Then, considering that not all cases had the status of all five biomarkers, we grouped the WSIs with a specific biomarker status into a dataset. At last, there were 831 WSIs from 485 cases for *1p/19q* codeletion and *MGMT* promoter methylation and 828 WSIs from 482 cases for *ATRX* mutation and *IDH1/2* mutation. For *TERT* promoter mutation, there were 489 WSIs from 266 cases. For each biomarker, we used 10-fold Monte Carlo cross-validation to divide the dataset into training, validation, and test sets under a split ratio of 8:1:1. Notably, WSIs from the same case were ensured to be included in the same set. Finally, we reported the pipeline's average prediction performance and the standard derivation on the test set.

In-house Xiangya Dataset

Our in-house Xiangya dataset contained 116 WSIs from 116 cases, where 94 WSIs were in the SDPC format, and 22 WSIs were in the QTIFF format. We converted the WSIs with SDPC format into the SVS format. Only *1p/19q* codeletion, *ATRX* mutation, *IDH1/2* mutation, and *MGMT* promoter methylation status were recorded in the Xiangya dataset. We pre-processed the WSIs as those in TCGA-LGG. Specifically, the *ATRX* mutation and *IDH1/2* mutation status of some cases were marked as indeterminate (neither positive nor negative), and we discarded these ambiguous labels. Finally, we constructed the Xiangya dataset containing 63 WSIs for *1p/19q* codeletion, 109 WSIs for *ATRX* mutation, 73 WSIs for *IDH1/2* mutation, and 64 WSIs for *MGMT* promoter methylation (Table 1).

Multi-Beholder Pipeline Design

Multiple Instance Learning Framework

As mentioned in the dataset description, each case in this study only had biomarker labels at the WSI level. Due to the giga-pixelated nature of WSI, it needed to be cut into patches whose labels could not be obtained. Therefore, the biomarker prediction problem was a typical weakly-supervised binary classification task. To this end, the MIL framework was employed in this paper. The MIL framework considered the WSIs as bags, denoted as $\{B_i\}$, where i stands for the index of the bags. Each bag was composed of K different instances (non-overlapping patches) denoted by $\{x_{i1}, x_{i2}, \dots, x_{iK}\}$ (K may vary across different WSIs). We only had access to the bag-level label Y_i but could not obtain the labels $\{y_{i1}, y_{i2}, \dots, y_{iK}\}$ of the instances.

The basic assumption of MIL is that if the label of a bag is positive ($Y_i = 1$), there is at least one instance in the bag whose label is positive as well. Otherwise, if the label of a bag is negative ($Y_i = 0$), all instances in the bag should have negative labels, i.e.,

$$Y_i = 1 \Leftrightarrow \exists y_{ij} = 1, j = 1, \dots, K \Leftrightarrow \max_j \{y_{ij}\} = 1, \quad (1)$$

$$Y_i = 0 \Leftrightarrow \forall y_{ij} = 0, j = 1, \dots, K \Leftrightarrow \max_j \{y_{ij}\} = 0. \quad (2)$$

This study considered codeletion, mutation, or methylation of a gene or a promoter as a positive label. Since each bag (WSI) corresponded to a specific biomarker status, they formed a sample point $\{B_i, Y_i\}$, where $Y_i \in \{0,1\}$.

Patch Feature Extraction

Because WSIs contain billions of pixels, the limitation of memory capacity in GPU makes it infeasible to directly input the WSIs into deep learning models. To significantly reduce the GPU memory occupation, we fed the instance features into the MIL framework instead of the patch images. Specifically, we first fed the patch $x_{ij} \in \mathbb{R}^{256 \times 256 \times 3}$ in each WSI into a ResNet50⁴⁸ network pre-trained on ImageNet⁴⁹ for feature extraction by

$$h_{ij} = \mathcal{F}(x_{ij}), \quad (3)$$

where $h_{ij} \in \mathbb{R}^{1024}$ is the extracted features, and \mathcal{F} is the ResNet50 network. After feature extraction, each WSI can be represented as a collection of feature vectors, i.e., $B_i = \{h_{i1}, h_{i2}, \dots, h_{iK}\}$.

Feature Refinement based on OCC

In the Multi-Beholder, the pre-trained ResNet50 based on natural images was used to extract pathological image features. However, the difference between natural and pathological images may lead to unsatisfactory feature extraction. To address this problem, we added a trainable feature refinement layer after ResNet50, which was composed of a fully connected (FC) layer with a ReLU activation function calculated by

$$z_{ij} = \text{ReLU}(\mathbf{W}^T h_{ij} + \mathbf{b}), \quad (4)$$

where $\mathbf{W} \in \mathbb{R}^{1024 \times 512}$ and $\mathbf{b} \in \mathbb{R}^{512}$ are the weights and bias of the FC layer, respectively. $\text{ReLU}(x) = \max(0, x)$ stands for the ReLU function, and $z_{ij} \in \mathbb{R}^{512}$ is the refined feature vector.

However, directly supervising the training of the feature refinement layer required accurate labels for the instances, which are not available under the MIL framework. To address this problem, we adopted the OCC strategy, which could make full use of the true negative instances in negative WSIs to obtain an accurate negative-positive decision boundary, thereby enabling the discrimination of negative and positive instances in the positive WSIs to assign instance precise pseudo-labels. Specifically, one-class support vector machine (OCSVM)⁵⁰ was used as the OCC model in the Multi-Beholder. Let $\{z_1^-, z_2^-, \dots, z_{N^-}^-\}$ be the set of refined instance features in the negative WSIs, where N^- represents the number of the instances in all negative WSIs. The basic idea of OCSVM is to find a hyperplane farthest to the zero point while ensuring all the training samples are on the same side of the normal vector of the hyperplane. In testing, the negative

instances are located on the side of the normal vector of the hyperplane, while the positive instances are located on the other side. The objective function of OCSVM is defined as

$$\min_{\mathbf{w}, \rho, \xi_i} \frac{1}{2} \|\mathbf{w}\|^2 - \rho + \frac{1}{\nu N^-} \sum_{i=1}^{N^-} \xi_i \quad (5)$$

s.t.

$$\langle \mathbf{w}, \Phi(z_i^-) \rangle \geq \rho - \xi_i, \quad 1 \leq i \leq N^-, \quad (6)$$

$$\xi_i \geq 0, 1 \leq i \leq N^-. \quad (7)$$

Here the projection function Φ was set to the identity function since the instance features z_i^- had become distinguishable through the feature refinement layer. \mathbf{w} and ρ are trainable parameters of the OCSVM, representing the normal vector and intercept of the hyperplane, respectively. ξ_i is the slack variable. Besides, $\nu \in (0,1]$ is a hyper-parameter used to determine an upper bound on the training error and a lower bound on the support vector ratio.

After training OCSVM utilizing equations (5)-(7), we could judge whether an instance in a positive WSI belongs to the negative category or not. Let B_i^+ be a testing positive bag composed of instances $\{z_{i1}^+, z_{i2}^+, \dots, z_{iK^+}^+\}$, where K^+ is the number of instances in the bag. The directed distance of each instance z_{ij}^+ to the hyper-plane \mathbf{w} without considering the intercept was calculated by

$$d_{ij} = \langle \mathbf{w}, \Phi(z_{ij}^+) \rangle. \quad (8)$$

The larger the directed distance, the higher the likelihood of the instance being negative. We defined the opposite value $\bar{d}_{ij} = -d_{ij}$ as the anomaly score for each instance in positive bags. Eventually, we could pseudo-label the instances in positive bags based on the anomaly scores. To ensure the accuracy of the pseudo-labels, we did not label all instances. Instead, we only selected the instances with the highest or lowest anomaly scores as confident instances and assigned them pseudo-labels. Specifically, all instances

were first sorted according to the anomaly score \bar{d}_{ij} . Then, the M instances with the minimum anomaly scores were labeled as negative, and those with the M maximum anomaly scores were annotated as positive. It is worth noting that some noisy patches, such as pen marks, shadows, and bubbles in the WSIs, were totally different from the tissue patches and had extremely high anomaly scores. Hence, we did not select patches corresponding to the highest anomaly score of r percentage, where r was a hyperparameter associated with the dataset.

For the negative WSIs, all instances are negative according to equation (2). Considering that we only assigned pseudo-labels to the confident instances in the positive WSIs, to ensure data balance, we only assigned negative labels to the top M and bottom M confident instances measured by the attention score in the negative WSIs.

With the pseudo-labeling strategy, we could assign labels to the confident instances in both positive and negative WSIs, which could be used as additional supervision samples for training the feature refinement layer, thereby improving the biomarker prediction performance. To take full advantage of instance-level supervision, we designed two separate instance classifiers for the negative and positive instances. The negative instance classifier classified negative and non-negative instances and vice versa. Specifically, the two classifiers were built by

$$\hat{y}_{ij}^- = \text{Softmax}(\mathbf{W}^{-\text{T}} z_{ij} + \mathbf{b}^-), \quad (9)$$

$$\hat{y}_{ij}^+ = \text{Softmax}(\mathbf{W}^{+\text{T}} z_{ij} + \mathbf{b}^+), \quad (10)$$

where $\mathbf{W}^- \in \mathbb{R}^{512 \times 2}$ and $\mathbf{W}^+ \in \mathbb{R}^{512 \times 2}$ are learnable weights, $\mathbf{b}^- \in \mathbb{R}^2$ and $\mathbf{b}^+ \in \mathbb{R}^2$ are learnable biases, and \hat{y}_{ij}^- and \hat{y}_{ij}^+ represent the probability of z_{ij} being a negative or positive instance, respectively.

Attention-Based Instance Aggregation

To predict the bag-level biomarker status, it is necessary to aggregate the feature representations of all instances in the bag to obtain a bag-level feature representation. Traditional instance aggregation operators in MIL include average pooling, max pooling, and others. However, these operators without trainable parameters have poor generalization. To address this issue, we adopted an attention-based feature aggregation method⁵¹. Technically, for each refined instance feature z_{ij} , denote its attention score to the bag-level feature as a_{ij} . The final bag-level feature representation was aggregated by the weighted average of all instance features over the attention scores by

$$Z_i = \sum_{j=1}^K a_{ij} \cdot z_{ij}, \quad (11)$$

where $Z_i \in \mathbb{R}^{512}$ is the aggregated bag-level feature representation. In this work, the attention score a_{ij} was obtained by the gated attention mechanism as

$$a_{ij} = \frac{\exp\{\mathbf{w}^T(\tanh(\mathbf{V}^T z_{ij}) \odot \text{sigmoid}(\mathbf{U}^T z_{ij}))\}}{\sum_{j=1}^K \exp\{\mathbf{w}^T(\tanh(\mathbf{V}^T z_{ij}) \odot \text{sigmoid}(\mathbf{U}^T z_{ij}))\}}, \quad (12)$$

where $\mathbf{w} \in \mathbb{R}^{D \times 1}$, $\mathbf{V} \in \mathbb{R}^{512 \times D}$, and $\mathbf{U} \in \mathbb{R}^{512 \times D}$ are learnable weights. D is a manually determined hyperparameter controlling the dimension of the latent features when calculating the attention scores.

After obtaining the bag-level representations, an FC layer activated by the Softmax function was utilized as the bag classifier to obtain the predicted probabilities of the biomarker status as

$$\hat{Y}_i = \text{Softmax}(\mathbf{W}_{\text{BAG}}^T Z_i + \mathbf{b}_{\text{BAG}}), \quad (13)$$

where $\mathbf{W}_{\text{BAG}} \in \mathbb{R}^{512 \times 2}$ and $\mathbf{b}_{\text{BAG}} \in \mathbb{R}^2$ are learnable weights and biases, respectively.

Optimization Objectives

We used cross entropy as the loss function for negative and positive instance classifiers. For an instance with pseudo-label y_{ij} , the loss of the negative instance classifier can be expressed as

$$L^-(z_{ij}) = -[(1 - y_{ij}) \log(\hat{y}_{ij}^-[1]) + y_{ij} \log(\hat{y}_{ij}^-[0])], \quad (14)$$

where $\hat{y}_{ij}^-[0]$ and $\hat{y}_{ij}^-[1]$, i.e., the first and second components of \hat{y}_{ij}^- , represent the predicted non-negative and negative evidence probability from the negative evidence classifier.

Similarly, the loss of the positive evidence classifier can be expressed as

$$L^+(z_{ij}) = -[y_{ij} \log(\hat{y}_{ij}^+[1]) + (1 - y_{ij}) \log(\hat{y}_{ij}^+[0])]. \quad (15)$$

The bag-level classifier also used the cross entropy loss, defined as

$$L^{\text{BAG}}(B_i) = -[Y_i \log(\hat{Y}_i[1]) + (1 - Y_i) \log(\hat{Y}_i[0])]. \quad (16)$$

For each WSI B_i , the total loss function was defined as the weighted sum of the losses of the instance classifiers and the bag-level classifier, which is expressed as

$$L(B_i) = \alpha_1 \cdot L^{\text{BAG}}(B_i) + \frac{\alpha_2}{2|C(B_i)|} \sum_{z_{ij} \in C(B_i)} L^-(z_{ij}) + L^+(z_{ij}). \quad (17)$$

Here $C(B_i)$ represents the features of the confident instances in B_i . $|\cdot|$ represents the cardinality of a set. α_1 and α_2 are manually set weights, which satisfy $\alpha_1 + \alpha_2 = 1$.

Test-Time Domain Generalization

Due to distinctions in ethnicity, staining, scanners, etc., there are often differences between the WSIs used in training and testing, leading to a substantial performance drop when a model trained on the source domain (training set) is directly applied to the target domain (test set). Domain adaptation (DA) effectively solves the inconsistency between the source and target domains⁵². However, traditional DA techniques require target domain data to take part in the training process. Therefore, if the model needs to be applied to a new dataset, retraining is necessary, which is time-consuming and severely limits the model's usability. In contrast, testing-time DG methods do not need target domain data during training, enabling the model to

generalize well to a new target domain without retraining⁵³. Consequently, the Multi-Beholder adopted the DG method T3A⁵⁴ into the biomarker prediction task.

Specifically, two support sets, $\mathbb{S}^{(0)}$ and $\mathbb{S}^{(1)}$, were maintained for negative and positive WSIs, respectively, with the initial element being the weight of the bag-level classifier corresponding to the biomarker label. Namely, for the weight of the trained bag-level classifier \mathbf{W}_{BAG} , we had

$$\mathbb{S}^{(i)} = \mathbf{W}_{BAG}[:, i] \in \mathbb{R}^{512}, i = 0, 1. \quad (18)$$

Next, for each test WSI B , we first fed it into the trained Multi-Beholder and got a raw prediction \tilde{Y} . Then, we normalized the bag representation and added it to the support set corresponding to \tilde{Y} , i.e.,

$$\mathbb{S}^{(\tilde{Y})} \leftarrow \mathbb{S}^{(\tilde{Y})} \cup \left\{ \frac{Z}{\|Z\|} \right\}, \quad (19)$$

where $\|\cdot\|$ represents the L-2 norm.

Finally, the average of each support set was calculated as the new weight for the bag classifier, and the actually predicted label \hat{Y} for B was calculated by

$$\hat{Y} = \operatorname{argmax}_i \left\{ \frac{\exp(\langle c_i, Z \rangle)}{\exp(\langle c_0, Z \rangle) + \exp(\langle c_1, Z \rangle)} \right\}, \quad (20)$$

where

$$c_i = \frac{1}{|\mathbb{S}^{(i)}|} \sum_{z \in \mathbb{S}^{(i)}} z, i = 0, 1. \quad (21)$$

In practice, considering the raw predictions may be wrong, only the features whose prediction probability entropy is below the C -th largest among the support set were considered in equation (21), where C is a hyperparameter.

Visualization of attention maps and instance feature distributions

To visualize the attention map and the t-SNE instance feature distribution map, we chose the trained Multi-Beholder with the best test AUROC among the ten folds on the TCGA-LGG dataset. Then, we randomly selected one WSI in the test set for visualization. For the attention map, we first calculated the raw attention scores of each patch feature z_{ij} by $\mathbf{w}^T(\tanh(\mathbf{V}^T z_{ij}) \odot \text{sigmoid}(\mathbf{U}^T z_{ij}))$, and then we scaled the raw attention scores to 0-1 by the Min-Max normalization. Finally, the instances whose normalized attention scores were among the largest 10% were selected for better visualization by applying a heatmap upon the WSI under $1 \times$ magnification.

For the visualization of the instance distribution map, we first reduced the refined instance features to two dimensions using t-SNE⁴². Then, we uniformly selected up to 2,000 instances for plotting. To draw the decision boundary of the OCC on the 2-dimension plot, we utilized the SVR⁴³ to estimate the decision boundary by feeding the dimension-reduced instance features and the instance labels predicted by the trained OCSVM into the SVR. For *ATRX* mutation and *TERT* promoter mutation, because there were too few or even no predicted negative instances, it was difficult to train the SVR. So, we did not plot the estimated decision boundary. The attention scores were normalized by Min-Max normalization among the selected instances in the instance feature distribution map.

Cell proportion calculation with HoverNet

To calculate the proportions of different cell types in the top 10% attended patches, we utilized the HoverNet⁴¹ pre-trained on the PanNuke^{55,56} dataset, which was composed of histopathology patches under different magnifications from 19 different tissues, including the brain tumor, with over 200,000 precise-labeled nuclei annotations. The PanNuke dataset was officially split into three folds. We trained the HoverNet using the first fold and validated the HoverNet on the second fold, with the third fold being the test set. Besides, it is worth noting that in a validation epoch, we randomly selected 200 samples from the

whole validation dataset to save time. Finally, the HoverNet with the best validation loss was selected as the model for cell proportion calculation, which achieved an average Dice score of 0.7929 on the test set.

Experimental Settings

During training the Multi-Beholder, the batch size was one and the dimension of the latent features during attention calculation, i.e., D , was set to 128. The learning rate was set to 0.0005. The optimizer was Adam⁵⁷, with β_1 and β_2 set to 0.9 and 0.999, respectively. The weight decay was set to 1e-4. Early stopping was used during training. After each epoch, the model was evaluated by the AUROC on the validation set. The training was stopped if the validation AUROC did not increase for ten consecutive epochs with the maximum number of epochs being 200. Finally, the model with the highest validation AUROC was taken for testing. Apart from normalizing the patches using the mean and variance of ImageNet, no data augmentation was used. The number of confident instances M was set to 8 for $1p/19q$ codeletion, $ATRX$ mutation, and $TERT$ promoter mutation. For $IDH1/2$ mutation and $MGMT$ promoter methylation, M was set to 16 and 64, respectively. The weight of the bag loss α_1 was set to 0.7 for $1p/19q$ mutation, $MGMT$ promoter methylation, and $TERT$ promoter mutation and $\alpha_1 = 0.9$ for $IDH1/2$ mutation. For $ATRX$ mutation, we set $\alpha_1 = 0.3$. The percentage of the noisy patches not selected for pseudo-labeling, r , was set to 5 and 10 for $1p/19q$ codeletion and $IDH1/2$ mutation, respectively, with $r = 20$ for other biomarkers. As for OCSVM, the lower bound of the support vector ratio v was set to 0.25 for $ATRX$ mutation and $IDH1/2$ mutation, and v was 0.55, 0.05, and 0.95 for $1p/19q$ codeletion, $MGMT$ promoter methylation, and $TERT$ promoter mutation, respectively. OCSVM training was stopped when the reduction in training loss was less than 0.0001. After each training epoch, OCSVM was retrained from scratch. Besides, we utilized T3A for $1p/19q$ codeletion and $ATRX$ mutation with the number of selected instances in the support set, C , set to 10 and 8 on the TCGA-LGG dataset, respectively.

Statistical information and experimental environment

All available WSIs that had enough tissue areas were included in the deep learning pipeline. In this study, all experiments were done on an Ubuntu 18.04LTS server with one RTX 3090 GPU. The Multi-Beholder was implemented by Pytorch 1.12.1 and Pytorch Lightning 1.6.3. Moreover, the SGDCOneClassSVM in scikit-learn was utilized to implement the OCSVM model. The Python environment was 3.8.13. All metrics, including AUROC, accuracy, recall (=sensitivity), precision, and F1 score, were calculated by TorchMetrics 0.9.3. All metrics were measured under a macro-averaged scheme except for the accuracy, which was micro-averaged. SVR and t-SNE were implemented by scikit-learn 1.1.1. All statistical analyses were done by scikit-learn 1.3.0. All experimental result figures were created by seaborn 0.12.2.

Data Availability

TCGA-LGG is a public dataset that can be accessed through the Genomic Data Commons Data Portal (<https://portal.gdc.cancer.gov/>), where the WSIs and the biomarker status can be obtained. Xiangya is an in-house private dataset available upon reasonable requests to the corresponding authors.

Code Availability

After acceptance, the codes for model development and result analysis, along with the trained model parameters, will be open-sourced on GitHub.

References

1. Ferlay, J., Parkin, D. M. & Steliarova-Foucher, E. Estimates of cancer incidence and mortality in Europe in 2008. *European Journal of Cancer* **46**, 765–781 (2010).
2. Weller, M. *et al.* Glioma. *Nat Rev Dis Primers* **1**, 1–18 (2015).

3. Houshyari, M., Hajalikhani, F., Rakhsha, A. & Hajian, P. A Comparative Study of Survival Rate in High Grade Glioma Tumors Being Treated by Radiotherapy Alone Versus Chemoradiation With Nitrosourea. *Glob J Health Sci* **7**, 33–38 (2015).
4. Weller, M. *et al.* Molecular neuro-oncology in clinical practice: a new horizon. *The Lancet Oncology* **14**, e370–e379 (2013).
5. Śledzińska, P., Bebyn, M. G., Furtak, J., Kowalewski, J. & Lewandowska, M. A. Prognostic and Predictive Biomarkers in Gliomas. *International Journal of Molecular Sciences* **22**, 10373 (2021).
6. Kan, L. K. *et al.* Potential biomarkers and challenges in glioma diagnosis, therapy and prognosis. *BMJ Neurology Open* **2**, (2020).
7. Yao, J. *et al.* Human IDH mutant 1p/19q co-deleted gliomas have low tumor acidity as evidenced by molecular MRI and PET: a retrospective study. *Sci Rep* **10**, 11922 (2020).
8. Louis, D. N. *et al.* The 2016 World Health Organization Classification of Tumors of the Central Nervous System: a summary. *Acta Neuropathol* **131**, 803–820 (2016).
9. Ohba, S., Kuwahara, K., Yamada, S., Abe, M. & Hirose, Y. Correlation between IDH, ATRX, and TERT promoter mutations in glioma. *Brain Tumor Pathol* **37**, 33–40 (2020).
10. Shaw, E. G. *et al.* Randomized Trial of Radiation Therapy Plus Procarbazine, Lomustine, and Vincristine Chemotherapy for Supratentorial Adult Low-Grade Glioma: Initial Results of RTOG 9802. *JCO* **30**, 3065–3070 (2012).
11. Everhard, S. *et al.* MGMT methylation: A marker of response to temozolomide in low-grade gliomas. *Ann Neurol*. **60**, 740–743 (2006).

12. Wang, Z. *et al.* MGMT promoter methylation in serum and cerebrospinal fluid as a tumor-specific biomarker of glioma. *Biomedical Reports* **3**, 543–548 (2015).
13. Dubbink, H. J. *et al.* Diagnostic Detection of Allelic Losses and Imbalances by Next-Generation Sequencing: 1p/19q Co-Deletion Analysis of Gliomas. *The Journal of Molecular Diagnostics* **18**, 775–786 (2016).
14. Reifenberger, G., Wirsching, H.-G., Knobbe-Thomsen, C. B. & Weller, M. Advances in the molecular genetics of gliomas — implications for classification and therapy. *Nat Rev Clin Oncol* **14**, 434–452 (2017).
15. Haase, S. *et al.* Mutant ATRX: uncovering a new therapeutic target for glioma. *Expert Opinion on Therapeutic Targets* **22**, 599–613 (2018).
16. Echle, A. *et al.* Deep learning in cancer pathology: a new generation of clinical biomarkers. *Br J Cancer* **124**, 686–696 (2021).
17. Tsai, P.-C. *et al.* Histopathology images predict multi-omics aberrations and prognoses in colorectal cancer patients. *Nat Commun* **14**, 2102 (2023).
18. Elmore, J. G. *et al.* Diagnostic concordance among pathologists interpreting breast biopsy specimens. *JAMA* **313**, 1122–1132 (2015).
19. Hiley, C. T. *et al.* Challenges in molecular testing in non-small-cell lung cancer patients with advanced disease. *Lancet* **388**, 1002–1011 (2016).
20. Chang, P. *et al.* Deep-Learning Convolutional Neural Networks Accurately Classify Genetic Mutations in Gliomas. *AJNR Am J Neuroradiol* **39**, 1201–1207 (2018).

21. Evans, A. J. *et al.* US Food and Drug Administration Approval of Whole Slide Imaging for Primary Diagnosis: A Key Milestone Is Reached and New Questions Are Raised. *Arch Pathol Lab Med* **142**, 1383–1387 (2018).
22. Aeffner, F. *et al.* Introduction to Digital Image Analysis in Whole-slide Imaging: A White Paper from the Digital Pathology Association. *Journal of Pathology Informatics* **10**, 9 (2019).
23. Bera, K., Schalper, K. A., Rimm, D. L., Velcheti, V. & Madabhushi, A. Artificial intelligence in digital pathology — new tools for diagnosis and precision oncology. *Nat Rev Clin Oncol* **16**, 703–715 (2019).
24. Cui, M. & Zhang, D. Y. Artificial intelligence and computational pathology. *Laboratory Investigation* **101**, 412–422 (2021).
25. Weltgesundheitsorganisation. *WHO classification of tumours of the central nervous system.* (International Agency for Research on Cancer, 2016).
26. Coudray, N. *et al.* Classification and mutation prediction from non–small cell lung cancer histopathology images using deep learning. *Nat Med* **24**, 1559–1567 (2018).
27. Echle, A. *et al.* Clinical-Grade Detection of Microsatellite Instability in Colorectal Tumors by Deep Learning. *Gastroenterology* **159**, 1406-1416.e11 (2020).
28. Schirris, Y., Gavves, E., Nederlof, I., Horlings, H. M. & Teuwen, J. DeepSMILE: Contrastive self-supervised pre-training benefits MSI and HRD classification directly from H&E whole-slide images in colorectal and breast cancer. *Medical Image Analysis* **79**, 102464 (2022).
29. Shamaï, G. *et al.* Deep learning-based image analysis predicts PD-L1 status from H&E-stained histopathology images in breast cancer. *Nat Commun* **13**, 6753 (2022).

30. Couture, H. D. *et al.* Image analysis with deep learning to predict breast cancer grade, ER status, histologic subtype, and intrinsic subtype. *npj Breast Cancer* **4**, 30 (2018).
31. Gamble, P. *et al.* Determining breast cancer biomarker status and associated morphological features using deep learning. *Commun Med* **1**, 1–12 (2021).
32. Rawat, R. R. *et al.* Deep learned tissue “fingerprints” classify breast cancers by ER/PR/Her2 status from H&E images. *Sci Rep* **10**, 7275 (2020).
33. Shboul, Z. A., Chen, J. & M. Iftekharuddin, K. Prediction of Molecular Mutations in Diffuse Low-Grade Gliomas using MR Imaging Features. *Sci Rep* **10**, 3711 (2020).
34. Chang, K. *et al.* Residual Convolutional Neural Network for the Determination of IDH Status in Low- and High-Grade Gliomas from MR Imaging. *Clinical Cancer Research* **24**, 1073–1081 (2018).
35. Korfiatis, P. *et al.* Residual Deep Convolutional Neural Network Predicts MGMT Methylation Status. *J Digit Imaging* **30**, 622–628 (2017).
36. Jiang, S., Zanazzi, G. J. & Hassanpour, S. Predicting prognosis and IDH mutation status for patients with lower-grade gliomas using whole slide images. *Sci Rep* **11**, 16849 (2021).
37. Liu, S. *et al.* Isocitrate dehydrogenase (IDH) status prediction in histopathology images of gliomas using deep learning. *Sci Rep* **10**, 7733 (2020).
38. Li, Z. *et al.* Vision transformer-based weakly supervised histopathological image analysis of primary brain tumors. *iScience* **26**, (2023).
39. Eckel-Passow, J. E. *et al.* Glioma Groups Based on 1p/19q, IDH, and TERT Promoter Mutations in Tumors. *N Engl J Med* **372**, 2499–2508 (2015).

40. Xu, J., Liu, F., Li, Y. & Shen, L. A 1p/19q Codeletion-Associated Immune Signature for Predicting Lower Grade Glioma Prognosis. *Cell Mol Neurobiol* **42**, 709–722 (2022).
41. Graham, S. *et al.* Hover-Net: Simultaneous segmentation and classification of nuclei in multi-tissue histology images. *Medical Image Analysis* **58**, 101563 (2019).
42. Maaten, L. van der & Hinton, G. Visualizing Data using t-SNE. *Journal of Machine Learning Research* **9**, 2579–2605 (2008).
43. Drucker, H., Burges, C. J. C., Kaufman, L., Smola, A. & Vapnik, V. Support Vector Regression Machines. in *Advances in Neural Information Processing Systems* vol. 9 (MIT Press, 1996).
44. The Cancer Genome Atlas Research Network. Comprehensive, Integrative Genomic Analysis of Diffuse Lower-Grade Gliomas. *N Engl J Med* **372**, 2481–2498 (2015).
45. Esteller, M. *et al.* Inactivation of the DNA-Repair Gene *MGMT* and the Clinical Response of Gliomas to Alkylating Agents. *N Engl J Med* **343**, 1350–1354 (2000).
46. Lu, M. Y. *et al.* Data-efficient and weakly supervised computational pathology on whole-slide images. *Nat Biomed Eng* **5**, 555–570 (2021).
47. Otsu, N. A Threshold Selection Method from Gray-Level Histograms. *IEEE Trans. Syst., Man, Cybern.* **9**, 62–66 (1979).
48. He, K., Zhang, X., Ren, S. & Sun, J. Deep Residual Learning for Image Recognition. in *2016 IEEE Conference on Computer Vision and Pattern Recognition (CVPR)* 770–778 (2016). doi:10.1109/CVPR.2016.90.
49. Deng, J. *et al.* ImageNet: A large-scale hierarchical image database. in *2009 IEEE Conference on Computer Vision and Pattern Recognition* 248–255 (2009). doi:10.1109/CVPR.2009.5206848.

50. Schölkopf, B., Williamson, R., Smola, A., Shawe-Taylor, J. & Platt, J. Support vector method for novelty detection. in *Proceedings of the 12th International Conference on Neural Information Processing Systems* 582–588 (MIT Press, 1999).
51. Ilse, M., Tomczak, J. & Welling, M. Attention-based Deep Multiple Instance Learning. in *Proceedings of the 35th International Conference on Machine Learning* 2127–2136 (PMLR, 2018).
52. Guan, H. & Liu, M. Domain Adaptation for Medical Image Analysis: A Survey. *IEEE Transactions on Biomedical Engineering* **69**, 1173–1185 (2022).
53. Wang, J. *et al.* Generalizing to Unseen Domains: A Survey on Domain Generalization. *IEEE Transactions on Knowledge and Data Engineering* **35**, 8052–8072 (2023).
54. Iwasawa, Y. & Matsuo, Y. Test-Time Classifier Adjustment Module for Model-Agnostic Domain Generalization. in *Advances in Neural Information Processing Systems* (eds. Ranzato, M., Beygelzimer, A., Dauphin, Y., Liang, P. S. & Vaughan, J. W.) vol. 34 2427–2440 (Curran Associates, Inc., 2021).
55. Gamper, J., Alemi Koohbanani, N., Benet, K., Khuram, A. & Rajpoot, N. PanNuke: An Open Pan-Cancer Histology Dataset for Nuclei Instance Segmentation and Classification. in *Digital Pathology* (eds. Reyes-Aldasoro, C. C., Janowczyk, A., Veta, M., Bankhead, P. & Sirinukunwattana, K.) 11–19 (Springer International Publishing, 2019). doi:10.1007/978-3-030-23937-4_2.
56. Gamper, J. *et al.* PanNuke Dataset Extension, Insights and Baselines. Preprint at <http://arxiv.org/abs/2003.10778> (2020).

57. Kingma, D. P. & Ba, J. Adam: A Method for Stochastic Optimization. Preprint at <https://doi.org/10.48550/arXiv.1412.6980> (2017).

Acknowledgements

This work was supported in part by the National Natural Science Foundation of China (62031023&62331011), in part by the Shenzhen Science and Technology Project (GXWD20220818170353009), and in part by the Fundamental Research Funds for the Central Universities (Grant No. HIT.OCEF.2023050).

Ethics declarations

Competing interests

The authors declare no competing interests in any commercial or financial relationships.

Supplementary Information

- Supplementary Fig. 1-7
- Ablation study on the Multi-Beholder's performance with or without OCC

Tables

Table 1 Statistics of TCGA-LGG and Xiangya external cohort

Dataset & Race		TCGA-LGG (Western)	Xiangya (China)
Number of cases		N = 491	N = 116
Age (Mean±Standard Deviation)		43.5±13.5	37.1±16.9
Survival Months (Mean±Standard Deviation)		24.2±29.7	-
Sex	Male	242 (49.3%)	60 (51.7%)
	Female	191 (38.9%)	55 (47.4%)
	Not Available	58 (11.8%)	1 (0.9%)
Subtype	Anaplastic astrocytoma	156 (31.8%)	6 (5.2%)
	Anaplastic diffuse astrocytoma		1 (0.9%)
	Diffuse astrocytoma		54 (46.6%)
	Pilocytic astrocytoma		11 (9.5%)
	Pilomyxoid astrocytoma		1 (0.9%)
	Xanthomatous astrocytoma		3 (2.6%)

	Others		9 (7.8%)
	Oligoastrocytoma	113 (23.0%)	0 (0.0%)
	Oligodendroglioma	164 (33.4%)	20 (17.2%)
	Ependymoma	0 (0.0%)	4 (3.4%)
	Ganglionic glioma	0 (0.0%)	3 (2.6%)
	Not Available	58 (11.8%)	4 (3.4%)
WHO Staging	Stage I	0 (0.0%)	13 (11.2%)
	Stage II	205 (41.8%)	92 (79.3%)
	Stage III	228 (46.4%)	6 (5.2%)
	Not Available	58 (11.8%)	5 (4.3%)
<i>1p/19q</i> codeletion	Codeleted	161 (32.8%)	19 (16.4%)
	Non-codeleted	330 (67.2%)	44 (37.9%)
	Not Available	0 (0.0%)	53 (45.7%)
<i>ATRX</i> mutation	Mutated	177 (36.0%)	33 (28.4%)
	Wild-type	311 (63.3%)	76 (65.5%)
	Intermediate	0 (0.0%)	5 (4.3%)
	Not Available	3 (0.6%)	2 (1.7%)
<i>TERT</i> promoter mutation	Mutated	122 (24.8%)	-
	Wild-type	148 (30.1%)	-
	Not Available	221 (45.0%)	-
<i>IDH1/2</i> mutation	Mutated	398 (81.1%)	44 (37.9%)
	Wild-type	90 (18.3%)	29 (25.0%)
	Intermediate	0 (0.0%)	2 (1.7%)
	Not Available	3 (0.6%)	41 (35.3%)
<i>MGMT</i> promoter methylation	Methylated	407 (82.9%)	26 (22.4%)
	Non-methylated	84 (17.1%)	38 (32.8%)
	Not Available	0 (0.0%)	52 (44.8%)